AIP Advances

Effects of cation stoichiometry on surface morphology and crystallinity of $ZnGeN_2$ films grown on GaN by metalorganic chemical vapor deposition

Cite as: AIP Advances **10**, 065302 (2020); https://doi.org/10.1063/1.5137767
Submitted: 03 April 2020 . Accepted: 07 May 2020 . Published Online: 01 June 2020

Md Rezaul Karim, Benthara Hewage Dinushi Jayatunga, Menglin Zhu, Rebecca A. Lalk, Olivia Licata, Baishakhi Mazumder, Jinwoo Hwang, Kathleen Kash, and Hongping Zhao

COLLECTIONS

Paper published as part of the special topic on Chemical Physics, Energy, Fluids and Plasmas, Materials Science and Mathematical Physics

ARTICLES YOU MAY BE INTERESTED IN

Deep level defects and cation sublattice disorder in $ZnGeN_2$
Journal of Applied Physics **127**, 135703 (2020); https://doi.org/10.1063/1.5141335

Design of InGaN-$ZnSnN_2$ quantum wells for high-efficiency amber light emitting diodes
Journal of Applied Physics **124**, 034303 (2018); https://doi.org/10.1063/1.5036949

MOCVD homoepitaxy of Si-doped (010) β-Ga_2O_3 thin films with superior transport properties
Applied Physics Letters **114**, 250601 (2019); https://doi.org/10.1063/1.5109678

© 2020 Author(s).

Effects of cation stoichiometry on surface morphology and crystallinity of $ZnGeN_2$ films grown on GaN by metalorganic chemical vapor deposition

Cite as: AIP Advances 10, 065302 (2020); doi: 10.1063/1.5137767
Submitted: 3 April 2020 • Accepted: 7 May 2020 •
Published Online: 1 June 2020

View Online

Export Citation

CrossMark

Md Rezaul Karim,[1] Benthara Hewage Dinushi Jayatunga,[2] Menglin Zhu,[3] Rebecca A. Lalk,[2] Olivia Licata,[4] Baishakhi Mazumder,[4] Jinwoo Hwang,[3] Kathleen Kash,[2] and Hongping Zhao[1,3,a)]

AFFILIATIONS

[1] Department of Electrical and Computer Engineering, The Ohio State University, Columbus, Ohio 43210, USA
[2] Department of Physics, Case Western Reserve University, Cleveland, Ohio 44106, USA
[3] Department of Materials Science and Engineering, The Ohio State University, Columbus, Ohio 43210, USA
[4] Department of Materials Design and Innovation, University at Buffalo, Buffalo, New York 14260, USA

[a)] **Author to whom correspondence should be addressed:** zhao.2592@osu.edu

ABSTRACT

$ZnGeN_2$ films were grown on GaN-on-sapphire templates via metalorganic chemical vapor deposition. Energy dispersive x-ray spectroscopy was used to estimate the Zn/(Zn + Ge) composition ratio in the films. This ratio decreased with an increase in growth temperature but increased with an increase in total reactor pressure or the Zn/Ge precursor flow rate ratio. Systematic mapping of these key growth parameters has allowed us to identify the growth window to achieve $ZnGeN_2$ with stoichiometric cation composition. Compositional and statistical analyses performed on data acquired from atom probe tomography provided insight into the local compositional homogeneity. The cations Zn and Ge did not demonstrate segregation or clustering at the sub-nanometer level. Based on x-ray diffraction 2θ–ω scan profiles and transmission electron microscope nano-diffraction patterns, the films with near-stoichiometric cation ratios were single crystalline with planar surfaces, whereas zinc-rich or zinc-poor films were polycrystalline with nonplanar surfaces. The growth direction of the single crystalline $ZnGeN_2$ films on GaN templates was along the c-axis. Room temperature Raman spectra showed features associated with the phonon density of states, indicating the presence of cation disorder in the lattice. A cathodoluminescence peak associated with transitions involving deep level defects was observed around 640 nm. The intensity of this peak increased by almost 2.5 times as the temperature was reduced to 77 K from room temperature. A similar peak was observed in the photoluminescence spectra collected at 80 K.

© 2020 Author(s). All article content, except where otherwise noted, is licensed under a Creative Commons Attribution (CC BY) license (http://creativecommons.org/licenses/by/4.0/). https://doi.org/10.1063/1.5137767

I. INTRODUCTION

$ZnGeN_2$, a ternary heterovalent II-IV-N_2 compound, has recently attracted growing interest for applications in light emitters[1–3] and photovoltaics,[4,5] thanks to its complementary properties to GaN.[6–9] Hypothetically, the ideal $ZnGeN_2$ structure can be derived from a GaN crystal by replacing every two Ga atoms by one Zn atom and one Ge atom. An ideal octet-rule-preserving unit cell of $ZnGeN_2$, in which every N atom is bonded with two Zn and two Ge atoms, will have the orthorhombic symmetry of either space group $Pna2_1$ (sometimes referred to instead as $Pbn2_1$, depending on the particular choice of principal axes) or $Pmc2_1$, with the first structure being the lower energy configuration.[4] Deviation from the ideal coordination of the cations around N will result in a locally octet-rule-violating wurtzite structure (space group $P6_3mc$).[4] Although the octet-rule-violating, fully cation-disordered wurtzite structure

has significantly higher predicted formation energy per formula unit than the ordered $Pna2_1$ or $Pmc2_1$ structures,[5] this situation may be achieved, for example, in a kinetically limited growth regime.[10] The lattice parameters for the ordered and disordered structures have been measured to be similar.[10] The lattice mismatch of the $Pbn2_1$ structure with GaN is less than 1%.[11] The orthorhombic $Pna2_1$ ($Pbn2_1$) $ZnGeN_2$ structure has a predicted bandgap very close to that of GaN (3.4 eV).[11] From the theoretical prediction based on first-principles calculations, the valence band of $ZnGeN_2$ can be as high as 1.1 eV above that of GaN at the heterointerface.[6,7] This large band offset has inspired novel designs for high quantum efficiency optoelectronic devices including green light-emitting diodes,[1] ultraviolet laser diodes,[2] and quantum cascade lasers.[3] On the other hand, the presence of cation disorder has been predicted to shrink the bandgap significantly, by up to almost 3 eV.[5,12] Such a cation-disorder-dependent bandgap can be useful for designing broadband solar absorbers,[5] although such experimental verification for $ZnGeN_2$ is still lacking.

Prior efforts on the synthesis of $ZnGeN_2$ include reports on (i) powder samples synthesized from the reaction of NH_3 and Zn_2GeO_4,[13,14] (ii) polycrystalline films grown by the reaction of a Cl_2–N_2–HCl mixture with Zn and Ge vapors,[15] (iii) powder samples synthesized under high pressure–high temperature conditions from a mixture of Zn_3N_2 and Ge_3N_4,[16] (iv) radio frequency sputtered polycrystalline films,[17] (v) vapor–liquid–solid (VLS) synthesis of polycrystalline $ZnGeN_2$[10,18,19] and single crystal rods/plates,[10,19] and (vi) metalorganic chemical vapor deposition (MOCVD) growth of single crystalline films on sapphire substrates with c-plane[19] and r-plane orientations.[20,21] Recently, we have reported a study on the MOCVD growth of single crystalline $ZnGeN_2$ films on c-, r-, and a-plane sapphire substrates.[22]

In this work, we have systematically investigated the MOCVD growth of $ZnGeN_2$ films grown on GaN templates with (0001) orientation. Key growth parameters such as growth temperature, total reactor pressure, and cationic precursor flow rates were mapped to determine their impacts on the cation stoichiometry of $ZnGeN_2$ films grown on closely lattice-matched GaN. The surface morphology and crystalline quality of the films showed strong correlation with the cation stoichiometry. Comprehensive material characterization indicated that the films are substantially disordered on the cation sublattice.

II. EXPERIMENTAL DETAILS

The $ZnGeN_2$ films were grown in a custom designed dual-chamber MOCVD system. GaN-on-sapphire templates with (0001) out-of-plane orientation were used as substrates. The substrates were ~3.5 μm to 4.5 μm thick and unintentionally doped with free electron concentrations in the range of low 10^{17} cm^{-3}. Diethylzinc (DEZn), germane (GeH_4), and ammonia (NH_3) were used as the precursors of Zn, Ge, and N, respectively. N_2 was used as the carrier gas. Samples were grown at temperatures between 600 °C and 775 °C with reactor pressures between 200 Torr and 500 Torr. The DEZn-to-GeH_4 molar flow rate ratio (II/IV ratio) ranged between 15 and 75. The NH_3 molar flow rate was kept at 178 mmol/min. The substrates were cleaned *ex situ* using acetone and isopropanol, rinsed with deionized water, and blown dry using nitrogen. Prior to epi-growth, the substrates were *in situ* annealed for 3 min at 900 °C under a combination of N_2 and NH_3 flow. Table I summarizes the growth conditions for a series of samples in this study.

The atomic percentages of Zn, Ge, and N in the $ZnGeN_2$ films were measured by energy dispersive x-ray spectroscopy (EDS). Surface morphologies of the films were investigated by field emission scanning electron microscopy (FESEM). The thicknesses of the films were estimated from cross-sectional SEM imaging. FEI Apreo LoVac analytical SEM was used for both the EDS measurements and the FESEM imaging. Atom probe tomography (APT) was used to investigate the compositional homogeneity of the cations using a CAMECA Local Electrode Atom Probe (LEAP) 5000 XR system. APT samples were analyzed at a base temperature of 50 K, a laser pulse energy of 15 pJ, and an average evaporation rate of 0.005 ions per laser pulse. APT needle-shaped specimens were prepared in an FEI Nova 200 Focused Ion Beam (FIB) using standard lift-out and annular milling techniques. A Bruker Icon 3 atomic force microscope (AFM) was used to measure the roughness of the films. X-ray diffraction measurements were performed to determine the crystallinity and growth direction of the films using Bruker D8 Discover XRD with the Cu Kα source. Crystalline quality was investigated by scanning tunneling electron microscope (STEM) imaging using a Thermofisher probe-corrected Titan STEM operated at 300 kV. Raman spectra were captured at room temperature using a Renishaw–Smiths detection combined Raman–IR microprobe and 785 nm excitation wavelength. Cathodoluminescence (CL) measurements were performed using a Thermo Fisher Quattro Environmental Scanning Electron Microscope (ESEM) equipped with a Horiba H-Clue CL detector. A 325 μm wavelength cw He–Cd laser was used as the excitation source for the photoluminescence (PL) measurements. The excitation laser power was ~1.4 mW. The excitation spot size was ~100 μm in diameter. The spectra were resolved using a 0.8 m

TABLE I. Growth temperature (T_G) in °C, total reactor pressure (P) in Torr, DEZn/GeH_4 molar flow rate ratio (II/IV ratio, $R_{II/IV}$), thickness in μm, Zn/(Zn + Ge) compositions, and rms roughness in nm measured for each labeled sample. The growth temperatures were measured by using a thermocouple. The error in Zn and Ge atomic percentages is ~3%–4%. The NH_3 molar flow rate was 178 mmol/min in each case. The growth duration was 60 min for samples A–I, 45 min for sample J, and 20 min for sample K.

Sample	T_G (°C)	P (Torr)	$R_{II/IV}$	t (μm)	$\frac{Zn}{Zn+Ge}$	rms roughness (nm)
A	700	500	25	1.04	0.45	...
B	650	500	25	1.13	0.50	5.4
C	600	500	25	1.12	0.54	...
D	600	350	25	1.10	0.51	...
E	600	200	25	0.45	0.50	2.7
F	650	500	20	1.00	0.49	...
G	650	500	15	0.90	0.45	...
H	730	500	45	1.40	0.50	7.2
I	775	500	75	1.22	0.50	...
J	660	500	25	...	0.47	...
K	735	500	75	0.40	0.50	2.6

© Author(s) 2020

double monochromator with 2 nm resolution and detected with a Burle C31034A UV-enhanced photon counting cooled photomultiplier tube.

III. RESULTS AND DISCUSSIONS

A. $ZnGeN_2$ cation stoichiometry and growth rates

To investigate the effects of MOCVD growth parameters, i.e., growth temperature (T_G), total reactor pressure (P), and group II/IV molar ratio ($R_{II/IV}$), on the stoichiometry and crystallinity of the $ZnGeN_2$ films, three sets of samples were grown while varying only one of these parameters at a time within a set. The total gas flow by volume was kept constant for all growth experiments. The effects of T_G, P, and $R_{II/IV}$ on Zn/(Zn + Ge) composition and film thickness are plotted in Figs. 1(a)–1(c). The cation-to-anion ratios were measured to be stoichiometric, within the measurement error. The incorporation rate of Zn into the crystal depends on the concentration of Zn adatoms on the growth surface. The adatom concentration is directly proportional to the pressure of Zn in the vapor phase (P^v_{Zn}) and the flow rate of Zn (J_{Zn}) but inversely proportional to the equilibrium vapor pressure of liquid Zn (P_{Zn}).[23] For the samples C, B, and A, as shown in Fig. 1(a), the Zn/(Zn + Ge) composition monotonically decreased from 0.54 to 0.45 with an increase in growth temperature from 600 °C to 700 °C. This decrease is attributed to the effect of the increase in the equilibrium vapor pressure of Zn with an increase in temperature. For example, the equilibrium vapor pressure of Zn increases to ~75 Torr at 700 °C from ~15 Torr at 600 °C.[24] The vapor pressure of Ge is ~11 orders of magnitude less than that of Zn over this temperature range. For the samples E, D, and C, as shown in Fig. 1(b), the Zn/(Zn + Ge) composition increased from 0.5 to 0.54 with an increase in total reactor pressure from 200 Torr to 500 Torr. This effect can be ascribed to the increase in the pressure of Zn in the vapor phase (P^v_{Zn}) with an increase in the total reactor pressure (P). Finally, the increase in the II/IV ratio from 15 to 25 (samples G, F, and B, respectively) led to the increase in the Zn/(Zn + Ge) composition from 0.45 to 0.5, as expected [Fig. 1(c)].

Atom probe tomography (APT) measurements were performed on a $ZnGeN_2$ film grown at T_G = 660 °C with P = 500 Torr and $R_{II/IV}$ = 25 (sample J). The Zn/(Zn + Ge) composition measured by APT was found to be 0.47. APT provided insight on the compositional homogeneity of Zn and Ge atoms across the cross section of the $ZnGeN_2$ films. 3D atom maps of Zn and Ge from APT data are shown in Fig. 2(a). Zn and Ge atoms are shown in violet and green dots, respectively, in the atom maps. Regions of interest are shown in Fig. 2(a) as blue cylindrical slices, labeled i–iii. These measure 20 nm in diameter in the x–y plane and 3 nm in thickness along the z axis. These regions were selected to generate two-dimensional contour plots (2DCPs) of the Zn-to-Ge ratio, as shown in Fig. 2(b). The assessment of the 2DCPs revealed relatively homogeneous distributions with a range of 0.8–1.0 Zn/Ge. Statistical analyses were performed within the regions of interest, boxed in black in Fig. 2(a), measuring 20 × 15 nm in the xz plane and 2 nm thick, to define the likelihood of segregation or clustering of Zn and Ge. Frequency distribution analyses (FDA) allowed for the comparison of the experimental distribution and a calculated binomial distribution for each species. The resulting distributions are shown in Fig. 2(c) along with

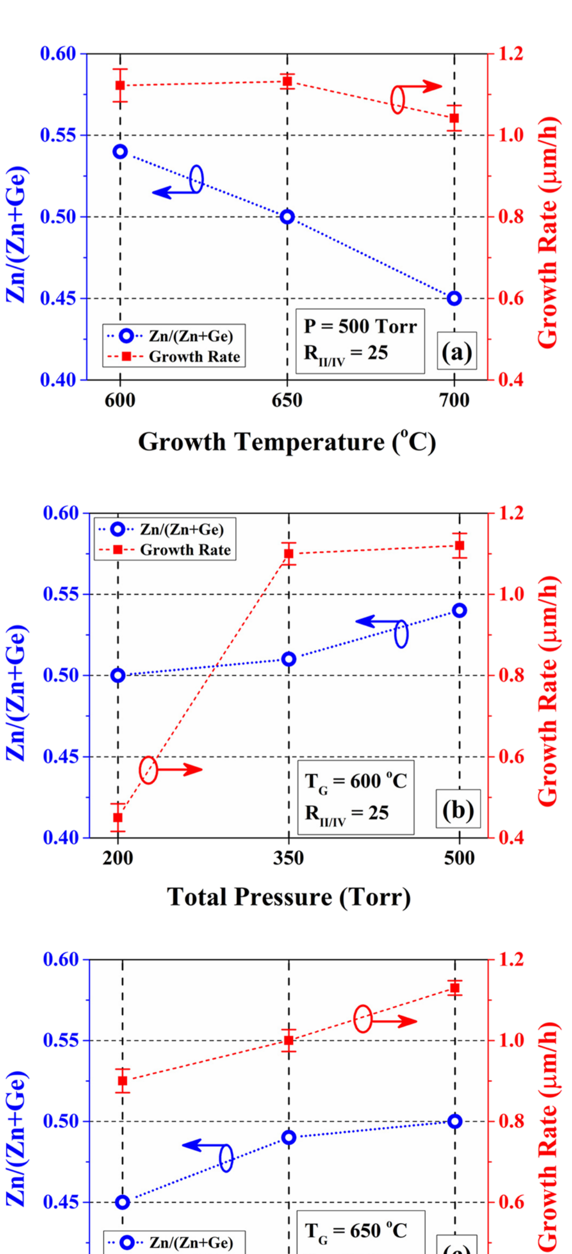

FIG. 1. The effects of (a) growth temperature T_G (samples A, B, and C), (b) total reactor pressure P (samples C, D, and E), and (c) II/IV ratio $R_{II/IV}$ (samples B, F, and G) on the Zn/(Zn + Ge) atomic composition and growth rate of the films. The atomic compositions were determined from EDS measurements. The error in Zn and Ge atomic percentages is ~3%–4%.

the statistical measurements of the Pearson coefficient (μ) and the probability-value (p-value). The binomial and experimental distributions are close, indicating a nearly random distribution. The μ reported here is independent of sample size and is analogous to a

© Author(s) 2020

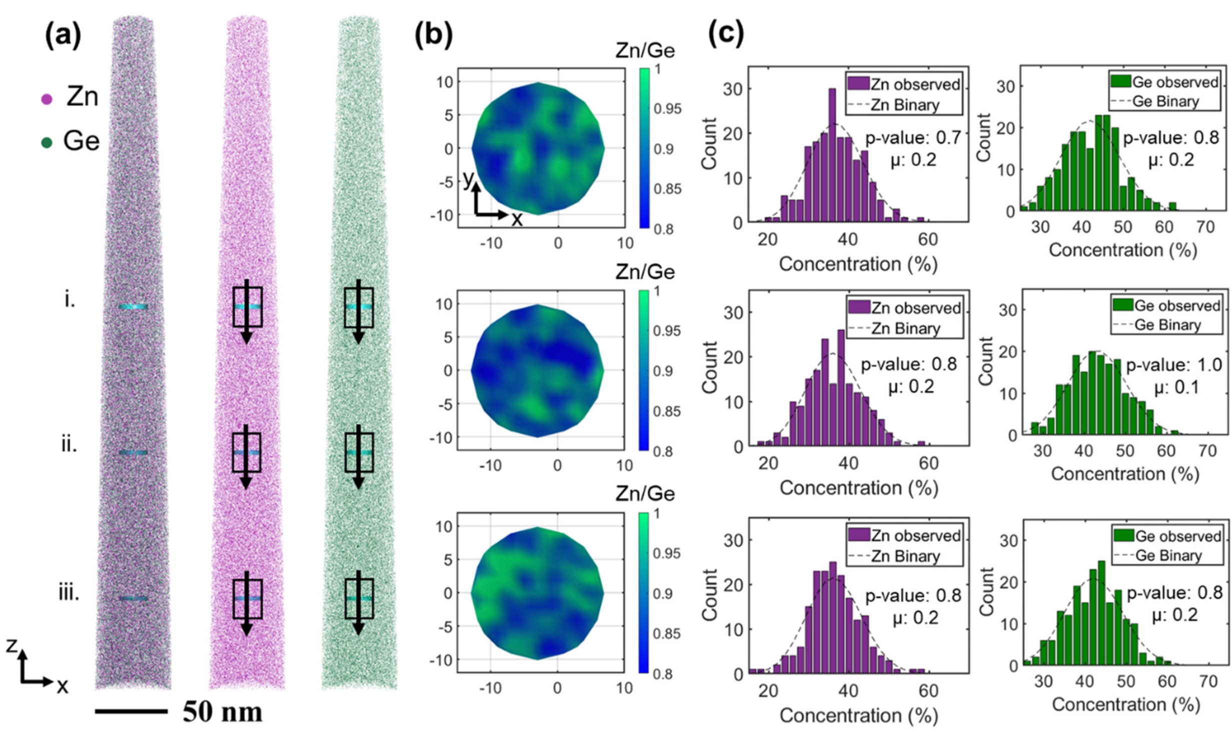

FIG. 2. (a) Three-dimensional atom maps of Zn (violet) and Ge (green) from the APT analysis of sample J (from left to right: Zn and Ge, Zn alone, and Ge alone). Three regions of interest are labeled i–iii and are shown as blue cylinders with the diameter of 20 nm and thickness of 3 nm. These regions were selected to generate (b) two-dimensional contour plots (2DCPs) of the Zn to Ge ratio. (c) Frequency of the experimental and calculated binomial distributions for Zn and Ge is plotted with the inset displaying the respective Pearson coefficient (μ) and probability-value (p-value). The regions of interest for the frequency distribution plots are shown as black boxes on the atom maps and have dimensions of 20 × 15 × 2 nm^3.

goodness of fit for which a value close to one indicates a complete association in the occurrence of the solute atoms and a value close to 0 indicates a random distribution. The p-value is a measure of confidence. A p-value of 0.01 indicates a confidence level of 99%. The p-value is not independent of sample size, and therefore, μ is the more reliable indicator for segregation. Both Zn and Ge demonstrate high p-values (close to 1) and low μ values, which indicate a lack of segregation or inhomogeneity. The combined analyses indicate a homogeneous distribution of Zn and Ge. Thus, there is no indication of the presence of a secondary phase, such as Zn_3N_2 or Ge_3N_4.

The growth rates of the $ZnGeN_2$ films were determined from cross-sectional SEM imaging. The measured values were in agreement with the estimated growth rates from the *in situ* reflectivity monitor. The error bars arise from the uncertainty due to the surface roughness plus the small variation in the thickness from the edge toward the center of the 2 in. wafer. With 500 Torr total pressure and a II/IV ratio of 25 (samples A–C), the growth rates of the films were close to 1.1 μm/hr. These growth rates did not vary significantly with the growth temperature [Fig. 1(a)]. At 600 °C, the growth rate remained almost constant (~1.1 μm/hr) as the total pressure decreased from 500 Torr to 350 Torr (sample D) but dropped to ~0.45 μm/hr at 200 Torr (sample E) [Fig. 1(b)]. On the other hand, for T_G = 650 °C and P = 500 Torr, the growth rate increased monotonically, from ~0.9 μm/hr to 1.1 μm/hr with an increase in the II/IV ratio from 15 to 25 (samples G, F, and B).

B. $ZnGeN_2$ surface morphologies and growth conditions

The plan-view FESEM images of the films shown in Fig. 1 are shown in Fig. 3. The surface morphologies of the films grown under otherwise identical conditions (P = 500 Torr and $R_{II/IV}$ = 25) but at T_G = 700 °C (sample A), 650 °C (sample B), and 600 °C (sample C) are plotted in Figs. 3(a)–3(c), respectively. Figures 3(d) and 3(f) show the films grown at T_G = 650 °C and P = 500 Torr [the same as the sample B in Fig. 3(b)] but with $R_{II/IV}$ = 20 (sample F) and 15 (sample G), respectively. The films shown in Figs. 3(e) and 3(g) were grown with chamber pressures of 350 Torr (sample D) and 200 Torr (sample E), respectively, but otherwise under the same conditions as the sample C shown in Fig. 3(c), with T_G = 600 °C and $R_{II/IV}$ = 25. From Fig. 1, it is understood that, depending on the combination of T_G, P, and $R_{II/IV}$, the grown film can be zinc-poor, stoichiometric, or zinc-rich. As seen here, the surfaces of the zinc-poor films [Figs. 3(a) and 3(f)] consist of facets aligned along certain preferred directions and the aspect ratios of the facets vary with growth conditions. In the case of zinc-rich films [Figs. 3(c) and 3(e)], the surfaces consist of crystallites of arbitrary shapes and

© Author(s) 2020

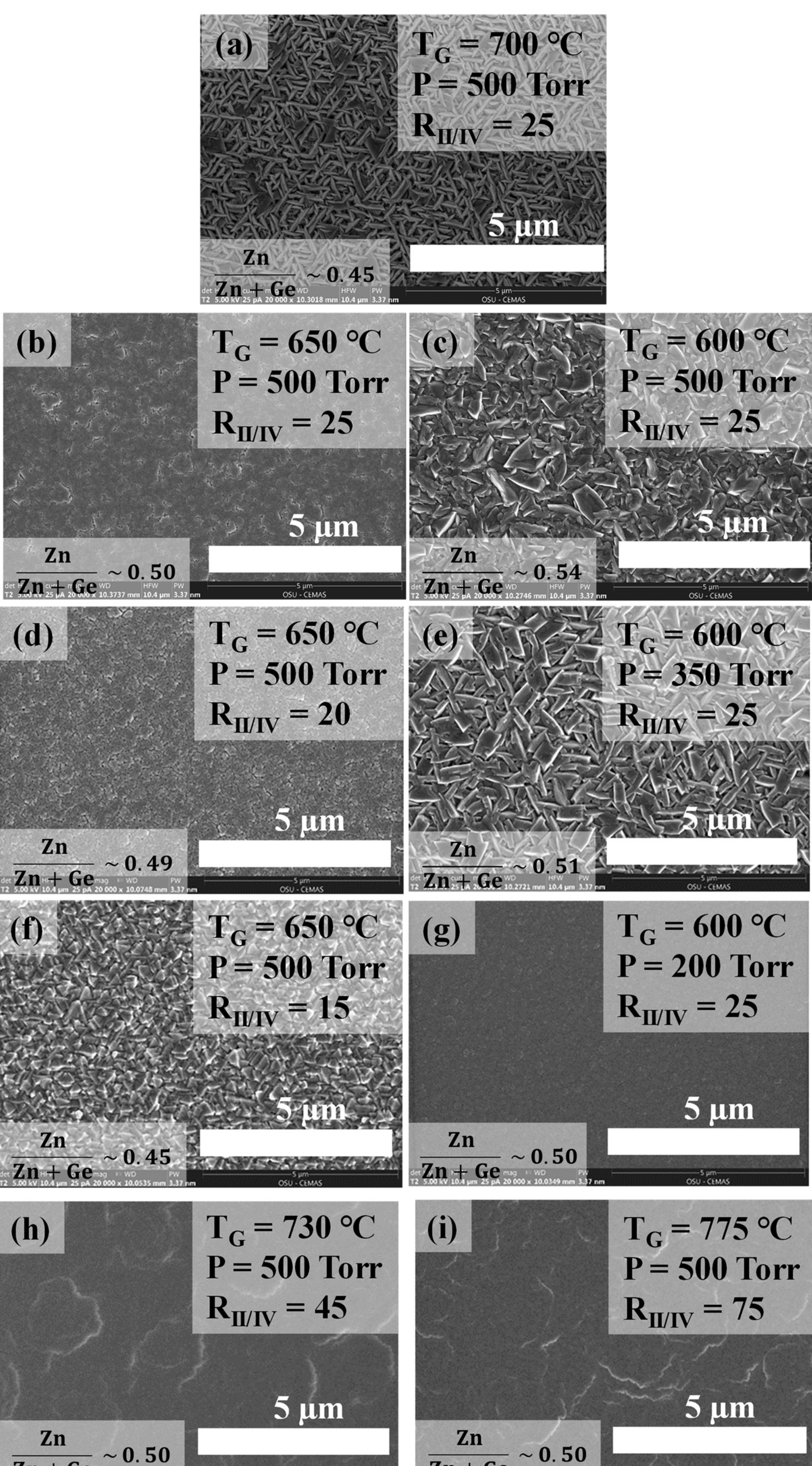

FIG. 3. Plan view FESEM images of the $ZnGeN_2$ films grown on GaN-on-sapphire templates. Films were grown with [(a)–(c)] P = 500 Torr, $R_{II/IV}$ = 25, and T_G = 700 °C (sample A), 650 °C (sample B), and 600 °C (sample C), respectively, [(d) and (f)] T_G = 650 °C, P = 500 Torr, and $R_{II/IV}$ = 20 (sample F) and 15 (sample G), respectively, and [(e) and (g)] T_G = 600 °C, $R_{II/IV}$ = 25, and P = 350 Torr (sample D) and 200 Torr (sample E), respectively. The Zn/(Zn + Ge) compositions in the films in panels (a)–(g) are also shown in Fig. 1. The growth parameters (T_G, P, and $R_{II/IV}$) for the films in panels (h) and (i) were (730 °C, 500 Torr, and 45) (sample H) and (775 °C, 500 Torr, and 75) (sample I), respectively.

© Author(s) 2020

sizes, without dominant orientations. Finally, the stoichiometric or near-stoichiometric films [Figs. 3(b), 3(d), and 3(g)] show planar surfaces, which evolved with growth temperature. Figures 3(h) and 3(i) are plan view FESEM images of two additional stoichiometric films grown at T_G = 730 °C (sample H: P = 500 Torr and $R_{II/IV}$ = 45) and T_G = 775 (sample I: P = 500 Torr and $R_{II/IV}$ = 75), respectively, showing larger features on the surface of the film grown at relatively higher temperatures. Figures 4(a)–4(c) show the 3D images obtained from the AFM scans of three stoichiometric $ZnGeN_2$ films grown at T_G = 600 °C (sample E), 650 °C (sample B), and 730 °C (sample H), respectively. The estimated film thicknesses and rms roughness values of these films were ~0.45 μm and 2.7 nm, ~1.1 μm and 5.4 nm, and ~1.4 μm and 7.2 nm, respectively. Figure 4(d) is an AFM image of a stoichiometric film grown at ~735 °C (sample K) but for only 20 min resulting in an estimated thickness of ~0.4 μm. The rms roughness value is ~2.6 nm, which is roughly 1/3 of that of the film grown at 730 °C but for 60 min [Fig. 4(c)]. In general, it was observed that for a similar growth temperature, the rms roughness increases as the film grows thicker. In addition, AFM images in Figs. 4(a)–4(c) indicate a gradual change in the dimensions of the surface features with the growth temperature. For 600 °C, the film surface [Fig. 4(a)] consists of needle-like features with vertical and lateral dimensions in the order of ~10 nm and ~200 nm, respectively. As the growth temperature increases, the feature sizes increase in both vertical and lateral dimensions. For the film grown at 730 °C, the surface is comprised of hillocks with average heights and widths of ~30 nm and 500 nm, respectively [Fig. 4(c)]. The evolution of the needle-like features to the hillocks is likely caused by the increased adatom mobility at elevated temperatures, facilitating the coalescence of adjacent structures. It is worthwhile noting that such evolution of surface features was observed regardless of the film thickness.

STEM imaging was carried out to better understand the mechanism causing the intriguing dependence of the surface morphology of the $ZnGeN_2$ films on Zn/(Zn + Ge) composition. The low angle annular dark field STEM (-LAADF) images of a Zn-rich (sample C) and a Zn-poor (sample A) film are shown in Figs. 5(a) and 5(b), respectively. The cross section of the Zn-rich film in Fig. 5(a) shows a columnar morphology. The columnar growth starts right from the interface between the substrate and the epifilm. The columnar cross-sectional morphology was also observed in the case of polycrystalline $ZnSnN_2$ films grown by combinatorial sputtering for a Zn/(Zn + Sn) composition between 0.45 and 0.7.[25] On the other hand, the dominant features of the cross section of a Zn-deficient film as shown in Fig. 5(b) are tilted filament-like structures, which give rise to the surface morphology shown in Fig. 3(a). Under highly Ge-rich growth conditions, the growth of rod-like structures is observed. This phenomenon may be caused by the presence of excess Ge on the growth surface. Figures 5(c)–5(e) represent the cross-sectional STEM-LAADF images of three near-stoichiometric films grown at T_G = 600 °C (sample E), 650 °C (sample B), and 775 °C (sample I), respectively. Either the total reactor pressure (P) or the II/IV ratio ($R_{II/IV}$) was varied to obtain near-stoichiometric cation compositions in these films. The near-stoichiometric films have more uniform cross sections than do the off-stoichiometric films. As the growth temperature increases, the

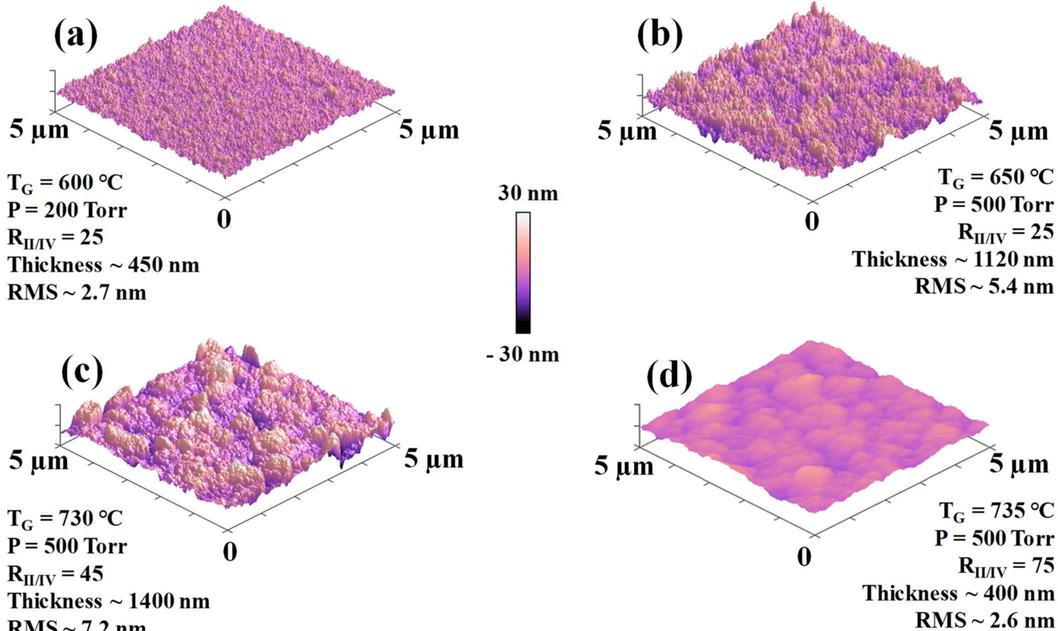

FIG. 4. 3D AFM images (45° rotated, 30° tilted) showing the evolution of the surface of stoichiometric $ZnGeN_2$ films with the increase in growth temperature. Films were grown at (a) 600 °C (sample E), (b) 650 °C (sample B), (c) 730 °C (sample H), and (d) 735 °C (sample K), respectively. Thicknesses of the films are 0.45 μm, 1.1 μm, 1.4 μm, and 0.4 μm, respectively. Either total reactor pressure or the II/IV molar ratio was adjusted to obtain stoichiometric films at different temperatures. The rms roughnesses of these films are 2.7 nm, 5.4 nm, 7.2 nm, and 2.6 nm, respectively.

© Author(s) 2020

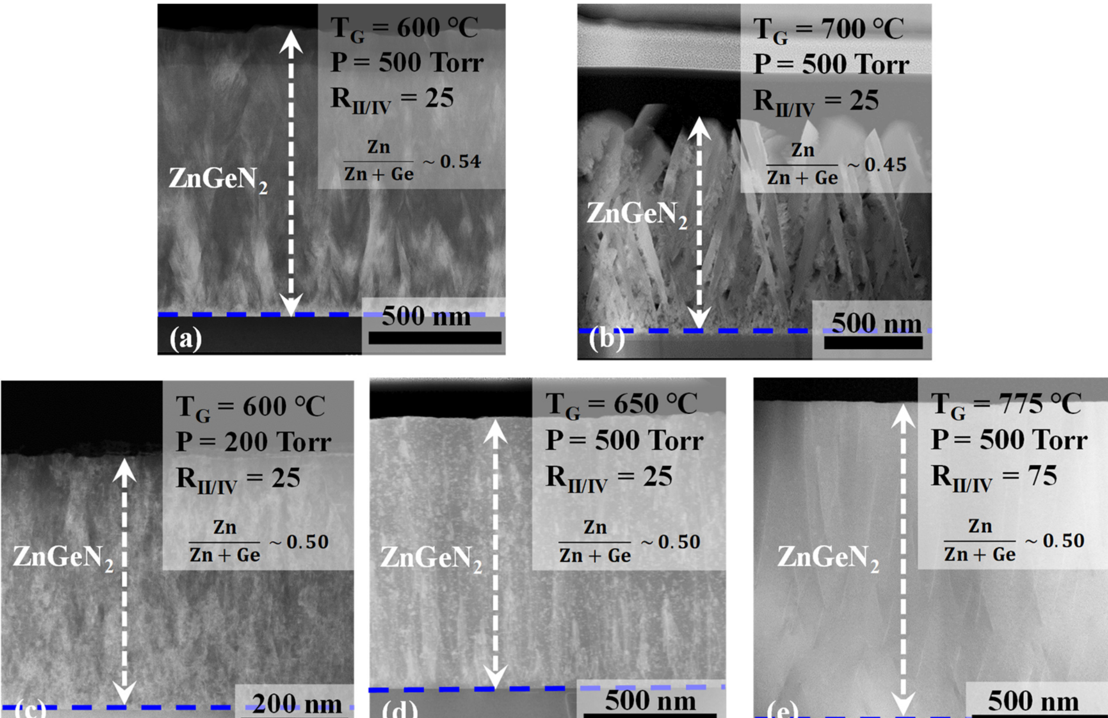

FIG. 5. STEM-LAADF images showing dramatically different cross-sectional morphologies in $ZnGeN_2$ films having different cationic compositions. The interfaces between the epi-film and the substrate were marked by blue dashed lines. These films are (a) zinc-rich (sample C), (b) zinc-poor (sample A), and [(c)–(e)] nominally stoichiometric (samples E, A, and I), respectively. For the samples showed in panels (c)–(e), either the total reactor pressure or the II/IV molar ratio was adjusted to obtain a nearly stoichiometric film at each of the different growth temperatures.

density of extended defects decreases. This effect is likely due to the higher mobility of the adatoms on the growth surface at elevated temperatures.

C. $ZnGeN_2$ crystallinity and crystal structures

Figures 6(a)–6(c) show the XRD 2θ–ω scan profiles obtained from a stoichiometric (sample B), a Zn-rich (sample C), and a Zn-poor (sample A) $ZnGeN_2$ film, respectively. In all cases, the highest intensity peak corresponds to the GaN (002) plane. For the stoichiometric film [Fig. 6(a)], the XRD 2θ–ω scan profile shows the strong $ZnGeN_2$ (002) peak at $2\theta = 34.64°$,[20,22] which has comparable intensity to the GaN (002) peak. No other $ZnGeN_2$ peak was observed between $2\theta = 20°$ and $90°$ except the $ZnGeN_2$ (004) peak at $2\theta = 73.07°$.[20,22] However, for the Zn-rich film [Fig. 6(b)], two 2θ–ω peaks at $2\theta = 32.42°$ and $36.72°$ positions are obvious, whereas the one at $2\theta = 36.72°$ position is noticeable for Zn-poor films [Fig. 6(c)]. These two peaks can be assigned to $ZnGeN_2$ (100) and (101) peaks, respectively, assuming a wurtzite structure.[26] It is likely that the intensity of the $ZnGeN_2$ (002) peak is low so that it overlaps with the GaN (002) shoulder in Figs. 6(b) and 6(c). The XRD 2θ–ω scan profiles in Fig. 6 indicate that stoichiometric films are single crystalline with (001) out-of-plane orientation, whereas Zn-rich or Zn-poor films are polycrystalline. Moreover, the positions of (002) and (004) peaks indicate that $ZnGeN_2$ has a slightly smaller lattice constant than GaN along the c-axis.

It is challenging to distinguish between the ordered ($Pna2_1$) and disordered ($P6_3mc$) $ZnGeN_2$ structures grown along the c-direction from the XRD 2θ–ω scan profiles because of the similar Bragg conditions of the primary planes of these polymorphs.[10] The TEM nano-diffraction patterns were used to investigate the crystallinity and crystal structures of the MOCVD grown films. A 15 × 15 array of nano-diffraction patterns was captured from ∼830 nm × 830 nm area from each investigated sample. In general, for the Zn-rich or Zn-poor films, substantial variations were observed among individual diffraction patterns in the array, whereas all 225 patterns were identical for nominally stoichiometric films. Moreover, the stoichiometric films grown under different growth conditions show very similar nano-diffraction patterns. Figures 7(a)–7(c) show the average of the 225 nano-diffraction patterns captured from a Zn-rich (sample C), a Zn-poor (sample A), and a stoichiometric $ZnGeN_2$ (sample I) film, respectively. These position-averaged diffraction patterns indicate that the near-stoichiometric films are single crystalline, whereas the off-stoichiometric films are polycrystalline in structure. In addition, the structural variations in the Zn-rich and Zn-poor films were markedly different, an observation associated with the different cross-sectional morphologies of these films [see Figs. 5(a) and 5(b)]. Figures 7(d) and 7(e) show two simulated

© Author(s) 2020

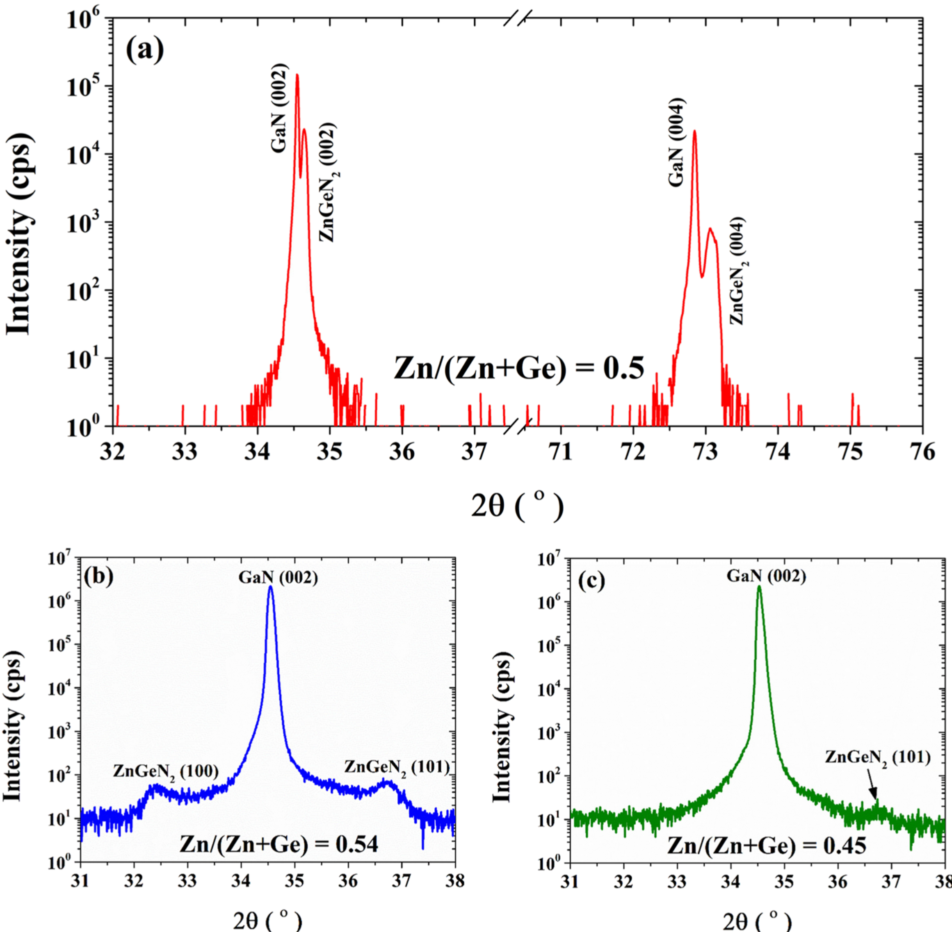

FIG. 6. XRD 2θ–ω scan-profile from a (a) stoichiometric (sample B), (b) Zn-rich (sample C), and (c) Zn-poor (sample A) $ZnGeN_2$ film. For the stoichiometric film, only {002} peaks were observed in the range of 2θ = 20°–90°. The growth parameters (T_G, P, and $R_{II/IV}$) were (650 °C, 500 Torr, and 25), (600 °C, 500 Torr, and 25), and (700 °C, 500 Torr, and 25), respectively.

electron diffraction patterns calculated assuming completely disordered $P6_3mc$ ([110] view direction) and ordered $Pna2_1$ ([100] view direction) structures, respectively, of $ZnGeN_2$. Hollow squares in Fig. 7(d) mark the space-group absences in the simulated pattern. Neither of these patterns adequately matches the experimental pattern in Fig. 7(c) to comment about the degree of disorder in the cation sublattice of the grown films. The experimental pattern is consistent with both the simulated diffraction patterns, except for the presence of the forbidden peaks, indicated by the open squares in Fig. 7(d). These forbidden peaks are also observed in the diffraction pattern of the underlying GaN template (not shown). Therefore, they most likely appear as a result of the inhomogeneous strain caused by the bending of the TEM lamella. Inhomogeneous strain can also be introduced by local variations in the distribution or ordering of the cations or by inhomogeneous stress in the lamella due to the lattice mismatch between the film and the substrate. Other important factors that can result in the appearance of additional diffraction spots are a thicker-than-ideal TEM lamella and amorphous layers on both sides of the lamella, as these conditions can potentially cause dynamical diffraction.

Figure 7(f) is a high magnification STEM image showing the alternating cation layers in a stoichiometric $ZnGeN_2$ film. For this lattice orientation, there should be equal distributions of Zn and Ge atoms in each cation column for both the fully ordered $Pna2_1$ phase and wurtzite-like random distributions of the cations. Therefore, we do not expect to obtain information on the degree of cation ordering from such an image. The contrast variation observed here could be a result of the presence of strain, crystalline defects, phase segregation, or non-uniform sample thickness.

Figure 8 shows the room temperature unpolarized Raman spectrum of a single crystalline stoichiometric $ZnGeN_2$ film (sample I, red curve), a Zn-rich film (sample C, blue curve), and a Zn-poor film (sample A, green curve) along with that of the GaN-on-sapphire template (black curve). A $ZnGeN_2$ unit cell has 78 optical phonon modes, all of which are Raman active.[27] None of these modes are seen here. The three narrow peaks observed in the spectrum are from phonon modes in the GaN template. In the case of the stoichiometric film, two broad features, one between 600 cm^{-1} and 700 cm^{-1} and the other around 830 cm^{-1}, are identified with peaks in the phonon density of states (DOSs) in $ZnGeN_2$.[19,28,29] These two features can also be seen, although they are less pronounced, in the spectrum from the Zn-rich film (blue curve). They are absent in the spectrum from the Zn-poor film (green curve). Cation disorder in $ZnGeN_2$, evident in x-ray diffraction spectra, has been shown to

© Author(s) 2020

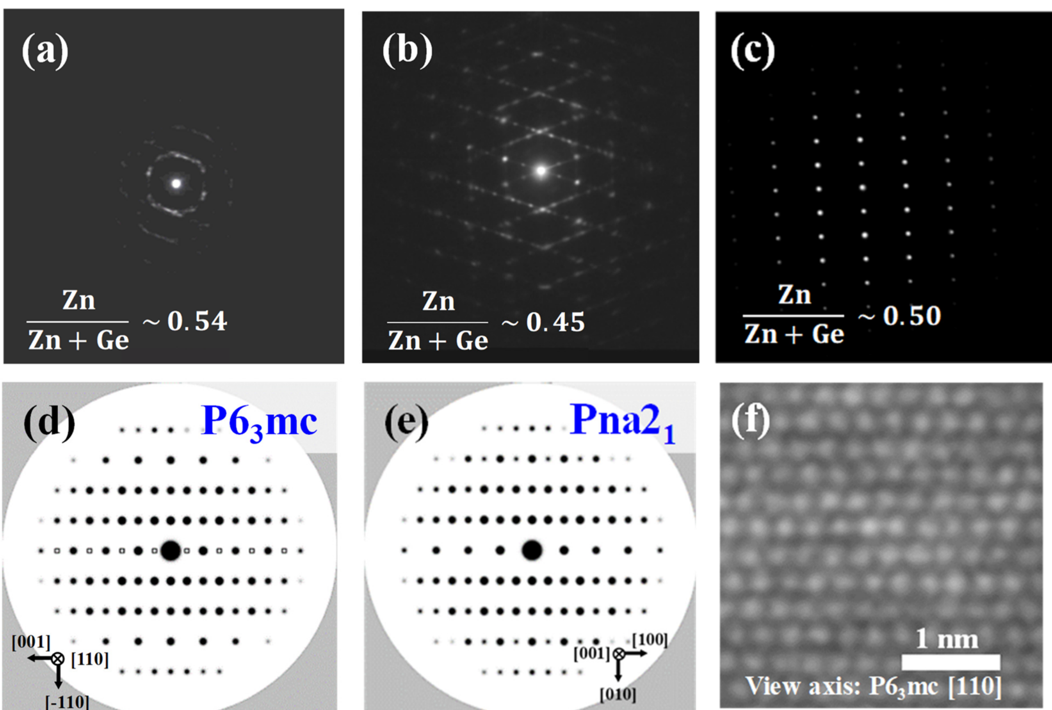

FIG. 7. Experimental position-averaged nano-diffraction patterns of (a) a Zn-rich (sample C), (b) a Zn-poor (sample A), and (c) a stoichiometric (sample I) $ZnGeN_2$ film, respectively. The growth parameters (T_G, P, and $R_{II/IV}$) were (600 °C, 500 Torr, and 25), (700 °C, 500 Torr, and 25), and (775 °C, 500 Torr, and 75), respectively. [(d) and (e)] Calculated TEM diffraction patterns of $ZnGeN_2$ assuming a $P6_3mc$ (wurtzite) structure and a $Pna2_1$ (orthorhombic) structure, respectively. (f) High magnification STEM imaging from the [110] view direction showing the alternating layers of cations.

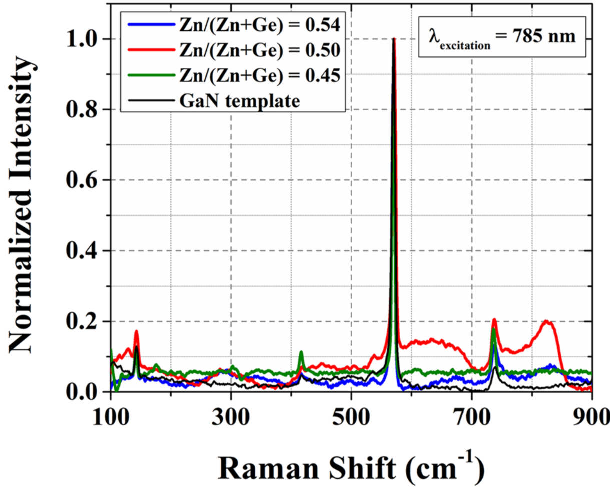

FIG. 8. Room temperature, unpolarized Raman spectra obtained from a Zn-rich (sample C, blue curve), a stoichiometric (sample I, red curve), and a Zn-poor (sample A, green curve) $ZnGeN_2$ film. The growth parameters (T_G, P, and $R_{II/IV}$) were (600 °C, 500 Torr, and 25), (775 °C, 500 Torr, and 75), and (700 °C, 500 Torr, 25), respectively. The Raman spectrum of the GaN-on-sapphire (black curve) is shown for comparison. A 785 nm laser was used as the excitation source. Each spectrum was normalized with respect to the corresponding intensity of the peak at 570 cm^{-1}.

lead to the relaxation of the momentum conservation rule and to the corresponding appearance of DOS features in the Raman spectra.[10] The absence of $ZnGeN_2$ Raman peaks in the spectrum in Fig. 8 is perhaps not surprising. In Ref. 10, the relative intensities of the Raman vs DOS peaks have been shown to increase for vapor–liquid–solid (VLS)-grown $ZnGeN_2$ on going from a growth temperature of 758–850 °C, with a corresponding change in the x-ray powder diffraction scan from disordered ($P6_3mc$) to ordered ($Pna2_1$). For the film shown in Fig. 8, the growth temperature is 775 °C, but the MOCVD growth process may be more kinetically limited than the very different, near-equilibrium VLS process, even for roughly the same growth temperatures.

D. $ZnGeN_2$ optical properties

Figure 9(a) shows the CL spectra of a stoichiometric $ZnGeN_2$ film grown at 730 °C (sample H) measured at three different temperatures (77 K, 123 K, and 298 K). The electron beam energy and beam current were set as 5 keV and 23 nA, respectively. The sampling area was the same in all cases. No CL peak was observed near the 3.4 eV predicted bandgap of orthorhombic $ZnGeN_2$, even at 77 K. At room temperature, a broad peak was observed centered at ~615 nm (2.02 eV). At lower temperatures, this broad peak shows clear splitting into two peaks, with one centered at ~560 nm (2.22 eV) and the other at ~640 nm (1.94 eV). The intensities of both peaks increase as the temperature decreases. We attribute these peaks to yellow-band

© Author(s) 2020

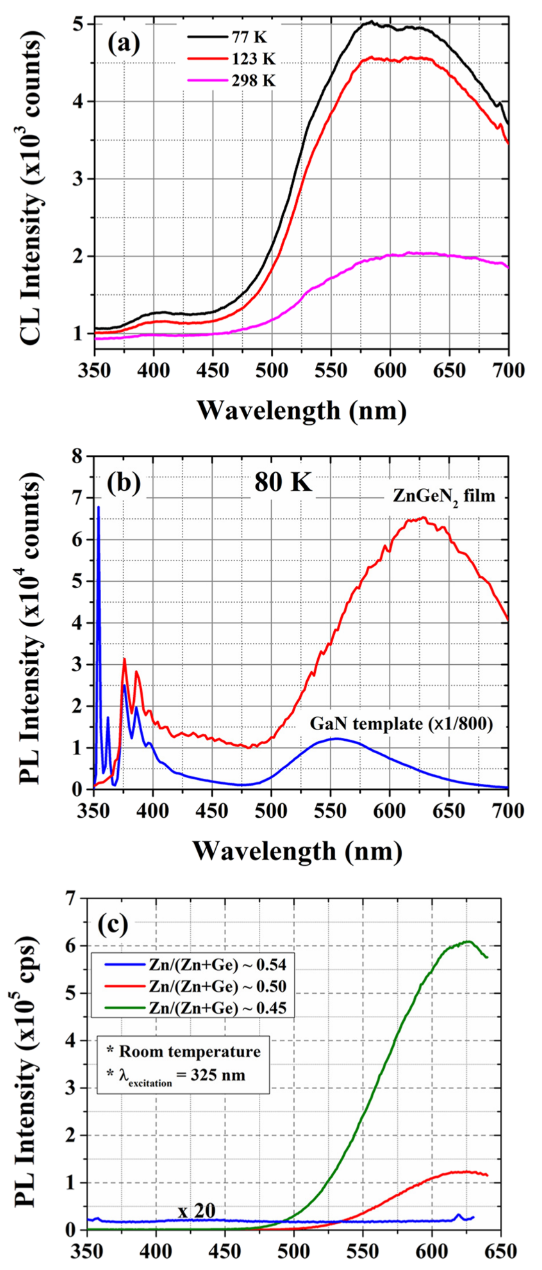

FIG. 9. (a) CL spectra measured at three different temperatures and (b) PL spectrum measured at 80 K of a stoichiometric $ZnGeN_2$ film grown at T_G = 730 °C, P = 500 Torr, and $R_{II/IV}$ = 45 (sample H). The PL spectrum of a GaN-on-sapphire template measured under the same conditions is shown in (b) for comparison. For the CL measurement, the electron beam energy and beam current were 5 keV and 23 nA, respectively. (c) Room temperature PL spectra measured from a Zn-poor (sample A), a stoichiometric (sample I), and a Zn-rich (sample C) film. The growth parameters (T_G, P, and $R_{II/IV}$) were (700 °C, 500 Torr, and 25), (775 °C, 500 Torr, and 75), (600 °C, 500 Torr, and 25), respectively. The intensity of the blue spectrum was multiplied by 20; the actual intensity is similar to the measured background level with an identical configuration. The blue curve shows very weak signals from the background.

luminescence (YBL)[30] from the underlying GaN template and from the $ZnGeN_2$ film. Similar peaks were observed in the room temperature PL spectra of $ZnGeN_2$ films grown on sapphire substrates.[22] Figure 9(b) shows the PL spectrum of the $ZnGeN_2$ film along with the PL spectrum of a GaN-on-sapphire template as a reference. Both spectra were measured at 80 K. From Fig. 9(b), it is evident that the peak centered at ~630 nm in the spectrum of the film (red) is primarily associated with the defect PL from the $ZnGeN_2$ layer, with possibly some contribution from the defect PL from the GaN substrate, whereas the peaks at wavelengths below 400 nm correspond to the near-band edge and impurity PL from the GaN substrate. Such "yellow-band-like" defect PL has been observed previously in $ZnGeN_2$ grown by VLS[18] and by MOCVD.[21,22] Figure 9(c) plots room temperature PL spectra collected from a Zn-poor (sample A), a stoichiometric (sample I), and a Zn-rich (sample C) film. The spectra from the Zn-poor and stoichiometric films show broad defect peaks at similar wavelengths near 625 nm, but no luminescence from the Zn-rich film was observed. This "yellow-band-like" luminescence may be related to Ge-at-Zn anti-site or Zn-vacancy-type defects.[31,32] However, further investigation such as defect spectroscopy is still required to confirm the origin of these defect levels.

IV. CONCLUSIONS

In conclusion, $ZnGeN_2$ films were grown by MOCVD on the closely lattice-matched GaN-on-sapphire templates. The stoichiometry of the films was found to be highly dependent on the growth parameters, including growth temperature, total reactor pressure, and the group II/IV molar ratio. This work has demonstrated that stoichiometric $ZnGeN_2$ films on GaN can be achieved in a wide growth window by tuning combinations of these key parameters. The crystallinity and surface morphologies of the films were found to be highly dependent on the stoichiometry. APT measurements indicated that the local distribution of cations at the sub-nanometer scale is homogeneous. Near-stoichiometric films were found to be single crystalline, with the planar surface morphology, whereas the Zn-rich or Zn-poor films were polycrystalline, with surfaces consisting of crystallites and facets. Room temperature Raman spectra support the presence of significant cation disorder in the crystal. The measured CL and PL peaks show PL from the $ZnGeN_2$ layer reminiscent of the "yellow band" PL commonly observed in GaN.

ACKNOWLEDGMENTS

The authors acknowledge partial funding support from the National Science Foundation (Grant No. DMREF-SusChEM-1533957) and the U.S. Department of Energy (Grant No. DE-EE0008718). Karim, Zhao, Zhu, and Hwang also acknowledge support from the Seed Grant from the Institute for Materials Research at the Ohio State University and the Center for Emergent Materials, an NSF-funded MRSEC under Award No. DMR-1420451.

DATA AVAILABILITY

The data that support the findings of this study are available from the corresponding author upon reasonable request.

© Author(s) 2020

REFERENCES

[1] L. Han, K. Kash, and H. Zhao, J. Appl. Phys. **120**, 103102 (2016).
[2] H. Fu, J. C. Goodrich, O. Ogidi-Ekoko, and N. Tansu, J. Appl. Phys. **126**, 133103 (2019).
[3] L. Han, C. Lieberman, and H. Zhao, J. Appl. Phys. **121**, 093101 (2017).
[4] P. C. Quayle, E. W. Blanton, A. Punya, G. T. Junno, K. He, L. Han, H. Zhao, J. Shan, W. R. L. Lambrecht, and K. Kash, Phys. Rev. B **91**, 205207 (2015).
[5] D. Skachkov, P. C. Quayle, K. Kash, and W. R. L. Lambrecht, Phys. Rev. B **94**, 205201 (2016).
[6] A. Punya and W. R. L. Lambrecht, Phys. Rev. B **88**, 075302 (2013).
[7] A. P. Jaroenjittichai, S. Lyu, and W. R. L. Lambrecht, Phys. Rev. B **96**, 079907(E) (2017).
[8] S. Lyu, D. Skachkov, K. Kash, E. W. Blanton, and W. R. L. Lambrecht, Phys. Status Solidi A **216**, 1800875 (2019).
[9] S. Lyu and W. R. L. Lambrecht, J. Phys. D: Appl. Phys. **53**, 015111 (2020).
[10] E. W. Blanton, K. He, J. Shan, and K. Kash, J. Cryst. Growth **461**, 38–45 (2017).
[11] A. Punya, T. R. Paudel, and W. R. L. Lambrecht, Phys. Status Solidi C **8**, 2492–2499 (2011).
[12] R. A. Makin, K. York, S. M. Durbin, N. Senabulya, J. Mathis, R. Clarke, N. Feldberg, P. Miska, C. M. Jones, Z. Deng, L. Williams, E. Kioupakis, and R. J. Reeves, Phys. Rev. Lett. **122**, 256403 (2019).
[13] M. Maunaye and J. Lang, Mater. Res. Bull. **5**, 793 (1970).
[14] R. Viennois, T. Taliercio, V. Potin, A. Errebbahi, B. Gil, S. Charar, A. Haidoux, and J.-C. Tédenac, Mater. Sci. Eng. B **82**, 45–49 (2001).
[15] W. L. Larson, H. P. Maruska, and D. A. Stevenson, J. Electrochem. Soc.: Solid State Sci. Technol. **121**, 1673–1674 (1974).
[16] T. Endo, Y. Sato, H. Takizawa, and M. Shimada, J. Mater. Sci. Lett. **11**, 424–426 (1992).
[17] S. Kikkawa and H. Morisaka, Solid State Commun. **112**, 513–515 (1999).
[18] K. Du, C. Bekele, C. C. Hayman, J. C. Angus, P. Pirouz, and K. Kash, J. Cryst. Growth **310**, 1057–1061 (2008).
[19] T. Peshek, S. Wang, J. Angus, and K. Kash, MRS Proc. **1040**, 1040-Q01-01 (2007).
[20] L. D. Zhu, P. H. Maruska, P. E. Norris, W. Yip, and L. O. Bouthillette, MRS Int. J. Nitride Semicond. Res. **4**(S1), 149 (1999).
[21] T. Misaki, T. Tsuchiya, D. Sakai, A. Wakahara, H. Okada, and A. Yoshida, Phys. Status Solidi C **0**, 188–191 (2002).
[22] M. R. Karim, B. H. D. Jayatunga, Z. Feng, K. Kash, and H. Zhao, Cryst. Growth Des. **19**, 4661–4666 (2019).
[23] K. Okamoto, H. Mawatari, K. Yamaguchi, and A. Noguchi, J. Cryst. Growth **98**, 630–636 (1989).
[24] R. E. Honig, RCA Review **18**, 195–204 (1957).
[25] A. N. Fioretti, A. Zakutayev, H. Moutinho, C. Melamed, J. D. Perkins, A. G. Norman, M. Al-Jassim, E. S. Toberer, and A. C. Tamboli, J. Mater. Chem. C **3**, 11017 (2015).
[26] A. Jain, S. P. Ong, G. Hautier, W. Chen, W. D. Richards, S. Dacek, S. Cholia, D. Gunter, D. Skinner, G. Ceder, and K. A. Persson, APL Mater. **1**, 011002 (2013).
[27] W. R. L. Lambrecht, E. Alldredge, and K. Kim, Phys. Rev. B **72**, 155202 (2005).
[28] T. R. Paudel and W. R. L. Lambrecht, Phys. Rev. B **78**, 115204 (2008).
[29] E. W. Blanton, M. Hagemann, K. He, J. Shan, W. R. L. Lambrecht, and K. Kash, J. Appl. Phys. **121**, 055704 (2017).
[30] M. A. Reshchikov and H. Morkoç, J. Appl. Phys. **97**, 061301 (2005).
[31] D. Skachkov, A. P. Jaroenjittichai, L.-Y. Huang, and W. R. L. Lambrecht, Phys. Rev. B **93**, 155202 (2016).
[32] N. L. Adamski, Z. Zhu, D. Wickramaratne, and C. G. Van de Walle, J. Appl. Phys. **122**, 195701 (2017).

© Author(s) 2020